Orientation-Dependent Ionic-Current Rectification in Colloidal Crystals

Santiago F. Bonoli,* Leandro L. Missoni,* Yamila A. Perez Sirkin,† and Mario Tagliazucchi‡
Universidad de Buenos Aires, Facultad de Ciencias Exactas y Naturales, Departamento de Química Inorgánica Analítica y Química Física e Instituto de Química, Física de Materiales, Medioambiente y Energía (INQUIMAE-CONICET), Ciudad Autónoma de Buenos Aires C1428, Argentina

(Received 16 December 2024; revised 18 February 2025; accepted 7 October 2025; published 3 November 2025)

Nonreciprocal transport (current rectification) in bulk materials is rarer and more complex than at interfaces. We theoretically demonstrate ion current rectification in binary superlattices of oppositely charged nanoparticles and show that this effect strongly depends on the direction of the applied electric field. We derive an equation that relates the symmetry elements of the superlattice to the directions where rectification is forbidden. This equation is used to analyze the conductivity of different superlattices obtained from the numerical solution of the Poisson-Nernst-Planck equations.

DOI: 10.1103/rlp5-v889

Current rectifiers have different conductivities for different polarities of the applied bias. For example, asymmetric nanopore and nanochannel membranes rectify ionic currents [1–5], which has enabled applications in sensors [6], energy conversion and desalinization [7], and iontronic logical elements [8,9]. On the other hand, nonreciprocal transport in a bulk medium is less common than at interfaces because it requires noncentrosymmetric crystalline materials. Electrical conductors exhibiting this phenomenon has been reported [10–12] and proposed for harvesting energy from oscillating electric fields [13]. This Letter explores for the first time a material exhibiting nonreciprocal ion transport: we theoretically demonstrate ionic current rectification (CR) for binary colloidal crystals of oppositely charged nanoparticles (NPs) [14,15] and show that it strongly depends on the orientation of the applied electric field. Noncentrosymmetric NP superlattices (required for bulk CR) have been already prepared [15–17] and there exists studies addressing ion transport in arrays of charged NPs [8,9,18–23] and thin NP membranes [24–26], which places the material we propose within the grasp of current technology. The main theoretical result of this Letter is an equation that states the symmetry conditions required for nonreciprocal transport in colloidal crystals, which we use to analyze the results of numerical calculations.

Our model system is a binary crystal of N_p positively and N_n negatively charged spherical NPs per unit cell of volume V; see Fig. 1(a). The colloids have Q_i positive ($i = p$) or negative ($i = n$) charges and a radius R_i. The charges are evenly distributed in a spherical shell of thickness H_i around the NP core (i.e., a charge layer), which models a thin polyelectrolyte brush or gel [27]. The crystal is immersed in a 1:1 electrolyte solution containing N_nQ_n cations and N_pQ_p anions per unit cell. Ions can access the solution around the particles and the shell surrounding the core, but not the NP cores. Ion transport is modeled using the Nernst-Planck equation

$$\mathbf{J}_i(\mathbf{r}) = -D_i[\nabla\rho_i(\mathbf{r}) + z_i\rho_i(\mathbf{r})\beta e\nabla\psi(\mathbf{r})], \tag{1}$$

and Poisson equation

$$\nabla^2\psi(\mathbf{r}) = -\frac{e[\rho_+(\mathbf{r}) - \rho_-(\mathbf{r}) + \rho_p(\mathbf{r}) - \rho_n(\mathbf{r})]}{\varepsilon} \tag{2}$$

see references [28–30], where $\mathbf{r} = (x, y, z)$ is a point in the space, $\beta = (k_BT)^{-1}$ (T is the temperature and k_B is the Boltzmann constant), e is the elemental charge, and ε is the dielectric permittivity, which is assumed to be position-independent. $\mathbf{J}_i(\mathbf{r})$, $\rho_i(\mathbf{r})$, D_i, and z_i are the local flux, number density, diffusion coefficient, and charge of the ion i (for $i = +, -$; $z_\pm = \pm 1$). $\rho_i(\mathbf{r})$ for $i = p, n$ is the number density of fixed charges in the shell around the NP core of type i at position $\mathbf{r}$. ψ is the electrostatic potential.

All sets of points $\mathbf{r}_1$ and $\mathbf{r}_2$ that are equivalent due to translational symmetry (periodic boundary conditions) have the same ionic concentrations and fluxes, $\rho_i(\mathbf{r}_1) = \rho_i(\mathbf{r}_2)$ and $\mathbf{J}_i(\mathbf{r}_1) = \mathbf{J}_i(\mathbf{r}_2)$. The total electric field can be split into a constant, externally applied field ($\mathbf{E}^{\text{ext}}$) and an internal component, i.e., $\mathbf{E} = -\nabla\psi = \mathbf{E}^{\text{int}} + \mathbf{E}^{\text{ext}}$. The internal component, $\mathbf{E}^{\text{int}}$, is generated by the charges of the ions and NPs, and thus it is a periodic function in the system, $\mathbf{E}^{\text{int}}(\mathbf{r}_1) = \mathbf{E}^{\text{int}}(\mathbf{r}_2)$ [30]. Using $\mathbf{E}^{\text{int}} = -\nabla\psi - \mathbf{E}^{\text{ext}}$ and integrating between points $\mathbf{r}_1$ and $\mathbf{r}_2$ results in the following boundary condition for the electrostatic potential:

*These authors contributed equally to this work.
†Contact author: yperezsirkin@qi.fcen.uba.ar
‡Contact author: mario@qi.fcen.uba.ar

$$\psi(\mathbf{r}_1) - \psi(\mathbf{r}_2) = \mathbf{E}^{\text{ext}} \cdot (\mathbf{r}_2 - \mathbf{r}_1)^{\text{T}}, \tag{3}$$

where the superscript "T" indicates the transpose, i.e., $\mathbf{r}^{\text{T}}$ is a column vector (vectors without this superscript are always row vectors). At points $\mathbf{r}_{\text{NP}}$ on the surface of the hard core, we enforce the zero-charge boundary condition, $\nabla\psi(\mathbf{r}_{\text{NP}}) \cdot \hat{\mathbf{n}}_{\text{NP}} = 0$, and null ionic fluxes, $\mathbf{J}_i(\mathbf{r}_{\text{NP}}) \cdot \hat{\mathbf{n}}_{\text{NP}} = 0$. Note that the zero-charge boundary condition is imposed on the surface of the hard core [black particle in Fig. 1(a)] because the fixed charges are distributed in the volume of the shell [see Eq. (2)], but there are no surface charges on the core. We model steady-state currents, and thus the continuity condition applies for the ionic fluxes, $\nabla \cdot \mathbf{J}_i(\mathbf{r}) = 0$. Finally, the boundary conditions for electrostatics defined above determine ψ up to an additive constant, so we set $\psi = 0$ in a fixed point of the unit cell.

The total current density is given by [30]

$$\mathbf{j} = \frac{e}{V} \int_{\text{unit cell}} [\mathbf{J}_+(\mathbf{r}) - \mathbf{J}_-(\mathbf{r})] d\mathbf{r}. \tag{4}$$

This equation involves a mean over the volume of the unit cell and it is only valid for periodic systems. In the Supplemental Material [31] we show that this expression provides exactly the same result as integrating the ionic fluxes across a normal surface (which is a more common approach) and discuss the advantages of using Eq. (4). In the following analysis, we will consider only the component of $\mathbf{j}$ in the direction of $\mathbf{E}^{\text{ext}}$, $j_{\parallel} = \mathbf{E}^{\text{ext}} \cdot \mathbf{j}^{\text{T}}/|\mathbf{E}^{\text{ext}}|$. Perpendicular components, which cannot be ruled out for noncentrosymmetric systems [13], were in all cases very small and close to the numerical error of the calculations.

We solved the Poisson-Nernst-Planck (PNP) system of equations using the finite element method implemented in COMSOL Multiphysics ® v5.4 [1,30]. All calculations used $D_+ = D_- = 1.0 \times 10^{-9}$ m^2/s, $T = 293.15$ K, and $\varepsilon = 10\varepsilon_0$. Further details about the calculations are provided in Supplemental Material [31] and Ref. [30].

We first exemplify bulk CR for a colloidal crystal of oppositely charged colloids with the zinc blende structure [Fig. 1(a)], a noncentrosymmetric colloidal crystal that has been experimentally obtained using different synthetic routes [15,17]. The choice of Q, H, and R ($R_+ = R_- =$ 5 nm, $H_+ = H_- = 1.5$ nm, $Q_+ = Q_- = 190.6$) results in a density of fixed charges in the shell (ρ_p, ρ_n) of 0.3 nm^{-3}, which is achievable with current synthetic methods for polyelectrolyte brushes [32]. Figure 1(b) shows $j_{\parallel}$ vs E^{ext} for two different directions of the applied field. CR is observed in the [111] direction [blue curve, the direction is indicated with blue arrows in Fig. 1(a)], but not in the [001] one (z axis, orange curve and arrows).

To quantify CR, we use the rectification factor $\alpha_{\text{CR}}(\mathbf{E}^{\text{ext}}) = |j_{\parallel}^{\text{open}}|/|j_{\parallel}^{\text{close}}|$. The currents $j_{\parallel}^{\text{open}}$ and $j_{\parallel}^{\text{close}}$ correspond to opposite directions of the applied field $\mathbf{E}^{\text{ext}}$.

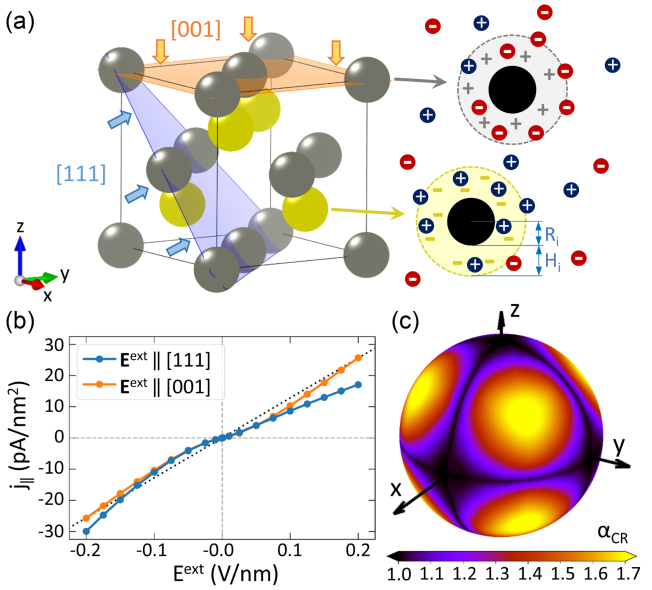

FIG. 1. (a) Crystal structure of zinc blende (space group $F\bar{4}3m$) showing the unit cell and the [001] and [111] directions for the applied potential. Positive and negative colloids are shown in gray and yellow, respectively. The inset schematizes the NP model: a solid core impenetrable to the ions (in black) is surrounded by a shell (permeable to the ions) having positive or negative fixed charges. (b) Current density as a function of the applied electric field plots for the directions shown in panel (a). The dotted line depicts an ideal ohmic (linear) response. (c) Color map of the CR factor, α_{CR}, calculated with the PNP equations as a function of the direction of the applied electric field (each direction of the applied field is represented as a point on the surface of the sphere) for $|\mathbf{E}^{\text{ext}}| = 0.2$ V/nm. Calculation parameters: $R_+ = R_- = 5$ nm, $H_+ = H_- = 1.5$ nm, and $Q_+ = Q_- = 190.6$.

Following the convention used in the nanopore literature [1,4,33], the "open" and "close" directions were chosen so that the former has always a larger current than the latter, i.e., $|j_{\parallel}^{\text{open}}| > |j_{\parallel}^{\text{close}}|$, and thus $\alpha_{\text{CR}} \geq 1$. While in nanopores $\mathbf{E}^{\text{ext}}$ is always normal to the membrane, in the present case $\mathbf{E}^{\text{ext}}$ can have any orientation with respect to the colloidal crystal. Figure 1(c) shows α_{CR} for the zinc blende colloidal crystal and different orientations of the applied field represented as a color map on the surface of a sphere. The plot reveals orientations displaying no CR ($\alpha_{\text{CR}} = 1$).

A key question is how the directions where CR is forbidden are related to the symmetry of the supercrystal. Let us consider a crystal having a symmetry operation (rotation, translation, reflection, or a combination of them), $\hat{\mathcal{T}}: \mathbf{r}^{\text{T}} \mapsto \mathsf{A}\mathbf{r}^{\text{T}} + \Delta\mathbf{r}^{\text{T}}$. Here, the vector $\Delta\mathbf{r}$ results in a translation and the matrix A accounts for reflections and rotations. For example,

$$\mathsf{A} = \text{diag}(1, 1, -1) = \begin{bmatrix} 1 & 0 & 0 \\ 0 & 1 & 0 \\ 0 & 0 & -1 \end{bmatrix} \tag{5}$$

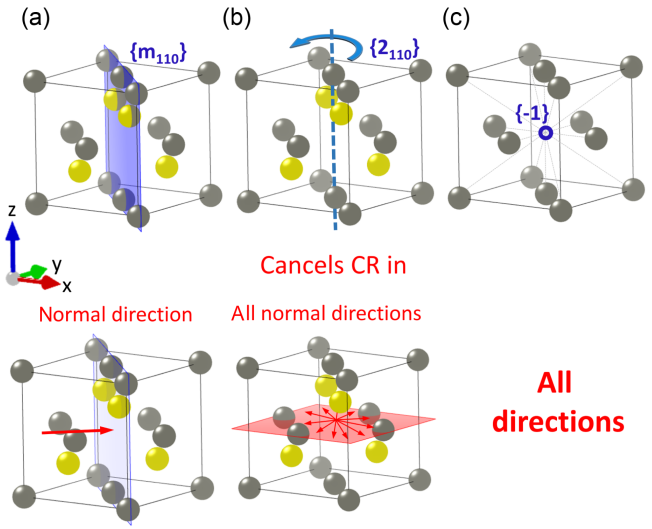

FIG. 2. Summary of the rules that relate symmetry operations to the directions of applied electric field for which current rectification is forbidden. The crystals shown in the example are zinc blende (a),(b) and fcc (c). (a) Reflection plane, (b) twofold rotation, and (c) inversion center.

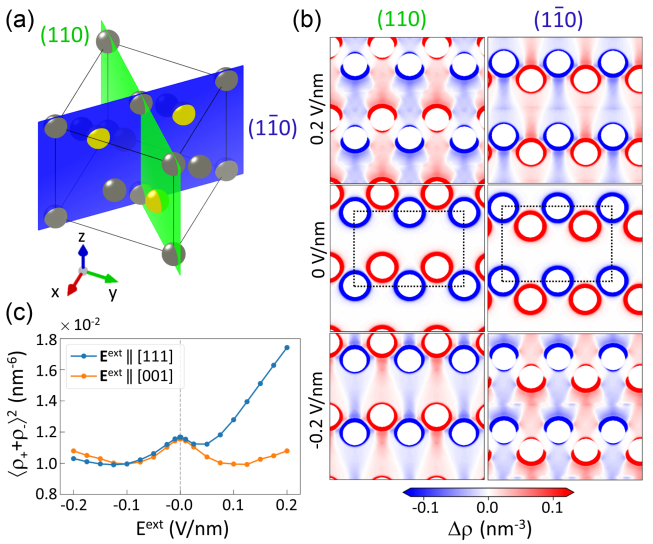

FIG. 3. (a) Scheme of the zinc blende structure showing the (110) and (1$\bar{1}$0) planes. (b) Color map of the net ionic charge density, $\Delta\rho$, along the (110) and (1$\bar{1}$0) planes obtained from PNP calculations for electric fields of −0.2, 0, and 0.2 V/nm applied in the [001] (z) direction. Regions in blue and red indicate a high concentration of negative and positive ions, respectively. (c) Mean squared total ion concentration vs E^{ext} for electric fields applied in the [001] direction (z, does not show CR, orange line) and the [111] direction (blue line, shows CR). Same calculation parameters as in Fig. 1.

converts the point (x, y, z) into $(x, y, -z)$ and, therefore, indicates a reflection in the xy plane. This reflection plane is denoted as $\{m_{001}\}$, where the subindex 001 indicates its Miller index. Applying $\hat{\mathcal{T}}$ to the PNP equations (1) and (2) (see End Matter) results in a simple equation that indicates the directions of the external field $\mathbf{E}^{\text{ext}}$ for which CR is forbidden,

$$\mathbf{E}^{\text{ext}}\mathsf{A} = -\mathbf{E}^{\text{ext}}. \tag{6}$$

This equation is the main result of this Letter and applying it to different crystallographic (space group) symmetry elements results in the following rules. (1) For reflection planes, CR is forbidden for $\mathbf{E}^{\text{ext}}$ normal to the plane; see example in Fig. 2(a). This rule also applies to glide planes (a glide plane is the combination of a reflection plane and a translation) because they have the same A as reflection planes. (2) For twofold rotation, CR is forbidden for all $\mathbf{E}^{\text{ext}}$ vectors perpendicular to the axis. A crystal having a twofold rotation axis remains invariable upon a 180° rotation around that axis. Figure 2(b), shows a twofold rotation axis aligned with the z axis, which transforms (x, y, z) to $(-x, -y, z)$. This axis is denoted as $\{2_{110}\}$ and has $\mathsf{A} = \text{diag}(-1, -1, 1)$. This rule also applies to twofold screw axes (a screw axis is the combination of a rotation and a translation) because they have the same A as twofold rotations. (3) In the presence of an inversion center, CR is forbidden in all directions; see Fig. 2(c). An inversion center ($\{-1\}$) transforms (x, y, z) to $(-x, -y, -z)$ and has $\mathsf{A} = \text{diag}(-1, -1, -1)$. Centrosymmetric lattices do not exhibit bulk current rectification. (4) Other symmetry operations (e.g., an n fold rotation axis $n \geq 3$, corresponding to a rotation of $360°/n$) do not eliminate CR.

Table S1 in [31] lists the symmetry elements, A matrices, and nonrectifying $\mathbf{E}^{\text{ext}}$ directions for zinc blende. The crystal has three twofold rotation axes parallel to the x, y, and z axes; therefore by Rule 2 CR is forbidden for external fields vectors laying on the yz, xz, and xy planes, in excellent agreement with the PNP numerical calculations in Fig. 1(b). The other symmetry elements of the blende structure (Table S1 [31]) do not cancel CR in additional directions. Interestingly, the maximum CR is obtained for $\mathbf{E}^{\text{ext}}$ aligned with the eight threefold rotation axes ($[\pm 1 \pm 1 \pm 1]$; see blue arrows in Fig. 1). We will return to this observation later.

Figure 3(a) shows the (110) and (1$\bar{1}$0) planes in the zinc blende structure. Figure 3(b) displays color maps of the net ionic charge density, $\Delta\rho(\mathbf{r}) = \rho_+(\mathbf{r}) - \rho_-(\mathbf{r})$, in those planes and different applied electric fields in the [001] direction (z direction, which does not exhibit CR). In equilibrium ($\mathbf{E}^{\text{ext}} = 0$), the ions adopt a symmetric distribution around the oppositely charged colloid. An electric field of 0.2 V/nm deforms the ionic clouds differently in the (110) and (1$\bar{1}$0) planes. The twofold rotation around the z axis ($\{2_{001}\}$ symmetry element) exchanges the (110) and (1$\bar{1}$0) planes and, therefore, the ion distribution in the (110) plane for $E^{\text{ext}} = 0.2$ V/nm is equivalent to that in the (1$\bar{1}$0) plane for $E^{\text{ext}} = -0.2$ V/nm and vice versa [Fig. 3(b)].

This result shows that if a crystal has a symmetry operation $\hat{\mathcal{T}}$, then the electrostatic potential $[\psi(\mathbf{r})]$ and the concentration of the ions $[\rho_i(\mathbf{r})]$ remain invariant after simultaneously applying $\hat{\mathcal{T}}$ and inverting the external electric field applied in a direction not exhibiting CR.

The symmetry in the distribution of ions shown in Fig. 3(b) is absent for $\mathbf{E}^{\text{ext}}$ in directions exhibiting CR. In those cases, there is a symmetry breaking in the ion distribution in the open and close states (the same phenomenon is responsible for CR in nanopores and nanochannels [1,4,33]). The mean squared total ion concentration, $\langle(\rho_+(\mathbf{r})+\rho_-(\mathbf{r}))^2\rangle$ (where $\langle\ldots\rangle$ indicates an average over the volume of the unit cell) is a simple parameter that reveals this asymmetry for directions displaying CR [blue line in Fig. 3(c)], while it exhibits a symmetry with the sign of the applied potential in nonrectifying cases [orange line in Fig. 3(c)].

Figure 4 provides an additional example of colloidal crystals with orientation-dependent CR. Wurtzite [Fig. 4(a)] is a hexagonal crystal system that has been predicted to be a stable phase for oppositely charged colloids [34]. The symmetry elements of wurtzite are compiled in Table S2 in [31]. The numerical solution of the PNP equations [Fig. 4(b)] shows the absence of CR for all $\mathbf{E}^{\text{ext}}$ vectors in the $(\vec{a},\vec{b})$ plane, in excellent agreement with symmetry predictions: wurtzite has a twofold screw axis in the $\vec{c}$ direction [known as $\{2_{001}|001/2\}$; see Fig. 4(a)], which negates CR in the whole plane normal to $\vec{c}$ (Rule 2). The other symmetry elements of wurtzite do not negate CR in additional directions.

Interestingly, Fig. 4(b) shows two regions of small rectification ($\alpha_{\text{CR}} \approx 1.02$–$1.06$, note the logarithmic scale) for electric fields with polar angles of $\theta \approx 0.2\pi$ and their reciprocal directions, $\theta \approx 0.8\pi$. While CR is very weak in these directions, it is still symmetry allowed. We explain this result by considering the local tetrahedral (Th) environment of the colloids. There are Th clusters in two different orientations in wurtzite [Fig. 4(c)]. Each cluster has three reflection planes with normals forming an angle of $\theta = \pi/2 - \gamma_{\text{Th}}/2 = 0.196\pi$ with respect to the $\vec{c}$ axis (where γ_{Th} is the Th angle, 109.5°). Therefore, an approximate "local" application of Rule 1 results in weak CR for six vectors with $\theta = 0.196\pi$ [these six vectors form a single ring-shaped region in Fig. 4(b) because of the resolution of the numerical calculations].

The local environment of the colloids also provides insights about the directions of maximum CR for wurtzite and zinc blende. Maximum CR in wurtzite [Fig. 4(b)] occurs in the [001] direction (c axis). In zinc blende, maximum CR is obtained in the $[\pm 1 \pm 1 \pm 1]$ directions (vectors passing through opposite corners of the cubic cell); see Fig. 1(a). Figures 4(d) and 4(e) show that all Th clusters in zinc blende and wurtzite have a threefold rotation axis in the direction of maximum CR. This is a reasonable result considering that the Th cluster has a highly asymmetric charge distribution along its threefold rotation axis.

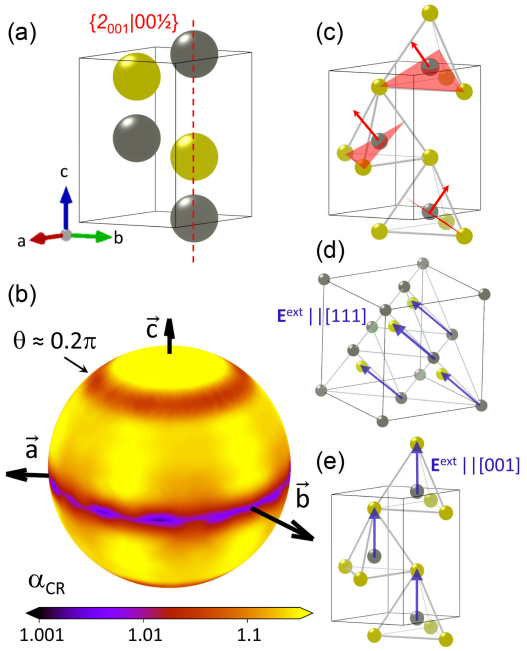

FIG. 4. (a) Wurtzite colloidal crystal (space group $P6_3mc$). Positive and negative colloids are shown in gray and yellow, respectively. (b) CR factor as a function of the direction of the applied field (note the logarithmic scale for α_{CR}). (c) Structure of wurtzite showing the tetrahedral clusters, examples of their reflection planes and their normal vectors. (d),(e) Structures of zinc blende (d) and wurtzite (e) showing the tetrahedral clusters and their threefold rotation axis (C_3) in the direction of maximum CR for each structure. Same calculation parameters as in Fig. 1. $V = 16384$ nm^3 for the unit cell shown in panel (a).

In Supplemental Material [31], we discuss a third example of CR, the case of the AuCl Cm, which only exhibits a reflection plane and, therefore, CR is only forbidden in directions normal to that plane (Rule 1). It is also interesting to explore the application of Eq. (6) to single nanopore membranes [1–5]. This calculation requires using in Eq. (6) the matrix A corresponding to the point symmetry group of the membrane (instead of the space group symmetry used for crystals) because nanopores are nonperiodic systems. The analysis predicts that a reflection plane normal to the pore axis or an inversion center negate CR, as previously proposed in the literature [35]. A more surprising result is that CR is also prohibited by any improper rotation axes normal to the membrane (an improper rotation, S_n, involves a rotation by an angle $360/n$ followed by a reflection in the plane normal to the rotation axis).

Regarding the possibility of experimentally observing bulk CR in colloidal crystals, our numerical calculations for 5 nm radius NPs require very large $|\mathbf{E}^{\text{ext}}|$ of ~0.1 V/nm. The mechanism of CR in oppositely charged colloidal crystals is analog to that in bipolar nanopores [1], where the rectification factor α_{CR} (for a constant applied potential bias) strongly increases when increasing the pore length

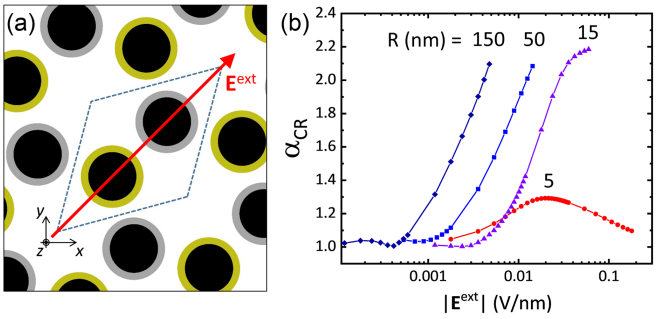

FIG. 5. (a) 2D noncentrosymmetric system (space group $P3m1$) used to study the effect of particle size on CR. The unit cell has an area A_{cell} and is indicated with dashed lines. The red arrow shows the direction of the applied electric field. Positive and negative colloids have the same properties (radius, R; shell thickness H; charge density in the shell ρ) and are shown in gray and yellow, respectively. (b) Effect of the magnitude of the applied electric field for different values of R at constant $H/R = 0.3$, $A_{\text{cell}}/R^2 = 0.0346$, and $\rho = 0.0084$ nm^{-3}.

because the size of the region where the ions can redistribute in nonequilibrium conditions is larger for long pores than for short ones [1]. We thus anticipate that the value of E^{ext} required for CR in colloidal crystals will decrease when increasing NP size. Fully 3D PNP calculations are prohibitive for $R > 5$ nm; hence we conducted calculations using a 2D system to test this hypothesis [Fig. 5(a), note the NPs in the 2D case are infinite core-shell cylinders in the z direction, but we expect the general trends to be valid for the 3D case as well]. Figure 5(b) shows that the threshold of $|\mathbf{E}^{\text{ext}}|$ required for CR decreases to $\sim$0.001 V/nm for $R = 150$ nm, suggesting that bulk CR can occur at experimentally accessible electric fields for large-enough NPs.

All results presented above employ a gap between NPs (which is required in 3D calculations to decrease the number of meshing elements), but, experimentally, colloidal crystals are packed structures of touching, immobile NPs. Figures S4(a) and S5(a) in Supplemental Material [31] show that α_{CR} increases when decreasing the gap between NPs and, thus, packed colloidal crystals exhibit CR. Figures S4(b) and S5(b) in [31] shows that decreasing the shell thickness, while keeping a constant charge, does not eliminate CR, suggesting that bulk CR can also achieved for NPs with surface charges instead of core-shell colloids.

In summary, we demonstrated ionic bulk CR in NP colloidal crystals. The translation symmetry of the material makes CR a more complex phenomenon than that observed in asymmetric nanopore membranes (i.e., interface CR). We developed symmetry arguments to predict the conditions where bulk CR is allowed (which can also be straightforwardly applied to interface CR) and numerically explored the phenomenon for colloidal crystals of oppositely charged NPs. Colloidal crystals exhibiting bulk CR do not require the bilayer architectures used in nanofluidic diodes [9,22,36], which may offer a fabrication advantage. A future research direction is exploring finite noncentrosymmetric colloidal crystals, which will simultaneously display both bulk and interface CR.

Acknowledgments—The authors acknowledge financial support from ANPCyT PICT-2021-I-INVI-00491 and CONICET (PIP 11220200102008C).

Data availability—The data that support the findings of this article are openly available [37].

[1] I. Vlassiouk, S. Smirnov, and Z. Siwy, ACS Nano **2**, 1589 (2008).
[2] Z. S. Siwy, Adv. Funct. Mater. **16**, 735 (2006).
[3] Z. Siwy and A. Fuliński, Phys. Rev. Lett. **89**, 198103 (2002).
[4] L.-J. Cheng and L. J. Guo, Chem. Soc. Rev. **39**, 923 (2010).
[5] A. Córdoba, J. M. M. de Oca, J. Dhanasekaran, S. B. Darling, and J. J. de Pablo, Mol. Syst. Des. Eng. **8**, 289 (2023).
[6] G. Pérez-Mitta, A. G. Albesa, C. Trautmann, M. E. Toimil-Molares, and O. Azzaroni, Chem. Sci. **8**, 890 (2017).
[7] K. Xiao, L. Jiang, and M. Antonietti, Joule **3**, 2364 (2019).
[8] T. M. Kamsma, J. Kim, K. Kim, W. Q. Boon, C. Spitoni, J. Park, and R. van Roij, Proc. Natl. Acad. Sci. U.S.A. **121**, e2320242121 (2024).
[9] X. Zhao, L. Yang, J. Guo, T. Xiao, Y. Zhou, Y. Zhang, B. Tu, T. Li, B. A. Grzybowski, and Y. Yan, Natl. Electron. Rev. **4**, 109 (2021).
[10] T. Ideue, K. Hamamoto, S. Koshikawa, M. Ezawa, S. Shimizu, Y. Kaneko, Y. Tokura, N. Nagaosa, and Y. Iwasa, Nat. Phys. **13**, 578 (2017).
[11] Y. Li, Y. Li, P. Li, B. Fang, X. Yang, Y. Wen, D.-x. Zheng, C.-h. Zhang, X. He, A. Manchon *et al.*, Nat. Commun. **12**, 540 (2021).
[12] T. Morimoto and N. Nagaosa, Sci. Rep. **8**, 2973 (2018).
[13] M. Suárez-Rodríguez, F. De Juan, I. Souza, M. Gobbi, F. Casanova, and L. E. Hueso, Nat. Mater. **24**, 1005 (2025).
[14] Y. Lin and M. Olvera de la Cruz, Proc. Natl. Acad. Sci. U.S.A. **120**, e2300257120 (2023).
[15] A. M. Kalsin, M. Fialkowski, M. Paszewski, S. K. Smoukov, K. J. Bishop, and B. A. Grzybowski, Science **312**, 420 (2006).
[16] Y. Zhang, D. D. Xu, I. Tanriover, W. Zhou, Y. Li, R. López-Arteaga, K. Aydin, and C. A. Mirkin, Nat. Photonics **19**, 20 (2025).
[17] M. Fujita, A. Toyotama, T. Okuzono, H. Niinomi, and J. Yamanaka, Soft Matter **20**, 985 (2024).
[18] Y. Yan, S. C. Warren, P. Fuller, and B. A. Grzybowski, Nat. Nanotechnol. **11**, 603 (2016).
[19] X. Zhao, B. Tu, M. Li, X. Feng, Y. Zhang, Q. Fang, T. Li, B. A. Grzybowski, and Y. Yan, Sci. Adv. **4**, eaau3546 (2018).
[20] J. Wang, L. Liu, J. Guo, X. Zhao, Y. Zhang, and Y. Yan, Adv. Funct. Mater. **34**, 2309531 (2024).
[21] Z. Chen, Y. Wang, W. Wang, and Z. Li, Appl. Phys. Lett. **95**, 102105 (2009).

[22] W. Ouyang, J. Han, and W. Wang, Lab Chip **17**, 3006 (2017).
[23] E. Choi, C. Wang, G. T. Chang, and J. Park, Nano Lett. **16**, 2189 (2016).
[24] S. Rao, K. J. Si, L. W. Yap, Y. Xiang, and W. Cheng, ACS Nano **9**, 11218 (2015).
[25] J. Cai, W. Ma, L. Xu, C. Hao, M. Sun, X. Wu, F. M. Colombari, A. F. de Moura, M. C. Silva, E. B. Carneiro-Neto *et al.*, Angew. Chem., Int. Ed. Engl. **58**, 17418 (2019).
[26] T. Xiao, J. Ma, Z. Liu, B. Lu, J. Jiang, X. Nie, R. Luo, J. Jin, Q. Liu, W. Li *et al.*, J. Mater. Chem. A **8**, 11275 (2020).
[27] M. Ballauff, Prog. Polym. Sci. **32**, 1135 (2007).
[28] M. Tagliazucchi and I. Szleifer, *Chemically Modified Nanopores and Nanochannels* (William Andrew, Oxford, 2016).
[29] R. B. Schoch, J. Han, and P. Renaud, Rev. Mod. Phys. **80**, 839 (2008).
[30] S. F. Bonoli, L. L. Missoni, Y. A. Perez Sirkin, and M. Tagliazucchi, J. Phys. Chem. C **128**, 25 (2024).
[31] See Supplemental Material at http://link.aps.org/supplemental/10.1103/rlp5-v889 for details of the numerical implementation of the Poisson-Nernst-Planck equations, tables of the crystallographic symmetry elements for the space groups used in this Letter, effect of interparticle gap and thickness of the charge shell on α_{CR}, details on the calculation of the mean ionic fluxes, and analysis of colloidal crystals with AuCl *Cm* structure.
[32] E. Spruijt, M. A. Cohen Stuart, and J. van der Gucht, Macromolecules **43**, 1543 (2010).
[33] M. Tagliazucchi, Y. Rabin, and I. Szleifer, ACS Nano **7**, 9085 (2013).
[34] A.-P. Hynninen, C. G Christova, R. Van Roij, A. Van Blaaderen, and M. Dijkstra, Phys. Rev. Lett. **96**, 138308 (2006).
[35] B. Riza Putra, L. Tshwenya, M. A. Buckingham, J. Chen, K. Jeremiah Aoki, K. Mathwig, O. A. Arotiba, A. K. Thompson, Z. Li, and F. Marken, Electroanalysis **33**, 1398 (2021).
[36] Y. Lei, W. Wang, W. Wu, and Z. Li, Appl. Phys. Lett. **96** (2010).
[37] S. F. Bonoli, L. L. Missoni, Y. A. Perez Sirkin, and M. Tagliazucchi, Data supplement for "Orientation-dependent ionic current rectification in colloidal crystals", https://github.com/softmatter-fcen/orientation-dependent-ionic-current-rectification-in-colloidal-crystals.

End Matter

Demonstration of Eq. (6)—Let us consider a crystal that is invariant after an Euclidean transformation (i.e., a rotation, translation, reflection, or a combination of them), $\hat{\mathcal{T}}:\mathbf{r}^{\mathrm{T}} \mapsto \mathsf{A}\mathbf{r}^{\mathrm{T}} + \Delta\mathbf{r}^{\mathrm{T}}$. In other words, the fixed charge of the colloids fulfills $\hat{\mathcal{T}}[\rho_i(\mathbf{r})] = \rho_i(\mathbf{r})$ $(i = p, n)$ and all boundary conditions are still fulfilled after the transformation. We now apply $\hat{\mathcal{T}}$ to the PNP equations (1) and (2), right multiply both terms of the Nernst-Planck equation [Eq. (1)] by A and use the following properties: (i) $\mathsf{A}^{\mathrm{T}}\mathsf{A} = \mathbb{I}$; (ii) $\hat{\mathcal{T}}[f(\mathbf{r})] = f(\hat{\mathcal{T}}[\mathbf{r}])$; (iii) $\hat{\mathcal{T}}[g(\mathbf{r})\nabla f(\mathbf{r})] = g(\hat{\mathcal{T}}[\mathbf{r}])\nabla f(\hat{\mathcal{T}}[\mathbf{r}])\mathsf{A}^{\mathrm{T}}$; (iv) $\hat{\mathcal{T}}[\nabla^2 f(\mathbf{r})] = \nabla^2 f(\hat{\mathcal{T}}[\mathbf{r}])$; and (v) $\hat{\mathcal{T}}:\mathbf{r} \mapsto \mathbf{r}\mathsf{A}^{\mathrm{T}} + \Delta\mathbf{r}$, which yields

$$\mathbf{J}_i(\hat{\mathcal{T}}[\mathbf{r}])\mathsf{A} = -D_i\left[\nabla\rho_i(\hat{\mathcal{T}}[\mathbf{r}]) + z_i\rho_i(\hat{\mathcal{T}}[\mathbf{r}])\beta e\nabla\psi(\hat{\mathcal{T}}[\mathbf{r}])\right], \tag{A1}$$

$$\nabla^2\psi(\hat{\mathcal{T}}[\mathbf{r}]) = -\frac{e[\rho_+(\hat{\mathcal{T}}[\mathbf{r}]) - \rho_-(\hat{\mathcal{T}}[\mathbf{r}]) + \rho_p(\mathbf{r}) - \rho_n(\mathbf{r})]}{\varepsilon}, \tag{A2}$$

and

$$\begin{aligned}\psi(\hat{\mathcal{T}}[\mathbf{r}_1]) - \psi(\hat{\mathcal{T}}[\mathbf{r}_2]) &= \mathbf{E}^{\mathrm{ext}}\cdot\hat{\mathcal{T}}[(\mathbf{r}_2 - \mathbf{r}_1)^{\mathsf{T}}] \\ &= \mathbf{E}^{\mathrm{ext}}\cdot\hat{\mathcal{T}}[\mathbf{r}_2^{\mathsf{T}} - \mathbf{r}_1^{\mathsf{T}}] \\ &= \mathbf{E}^{\mathrm{ext}}\cdot[\mathsf{A}(\mathbf{r}_2 - \mathbf{r}_1)^{\mathsf{T}}].\end{aligned} \tag{A3}$$

Comparing these equations with Eqs. (1)–(3) shows that for an applied field equal to $\mathbf{E}^{\mathrm{ext}}\mathsf{A}$, Eqs. (A1)–(A3) admit the solution $\psi(\hat{\mathcal{T}}[\mathbf{r}]) = \psi(\mathbf{r})$, $\rho_\pm(\hat{\mathcal{T}}[\mathbf{r}]) = \rho_\pm(\mathbf{r})$, and $\mathbf{J}_\pm(\hat{\mathcal{T}}[\mathbf{r}])\mathsf{A} = \mathbf{J}_\pm(\mathbf{r})$. Inserting the latter condition into Eq. (4) results in an average current $\mathbf{j}\mathsf{A}$ and a component of the current in the direction of the field equal to $\mathbf{E}^{\mathrm{ext}}\cdot(\mathbf{j}\mathsf{A})^{\mathrm{T}}/|\mathbf{E}^{\mathrm{ext}}| = \mathbf{E}^{\mathrm{ext}}\cdot(\mathsf{A}^{\mathrm{T}}\mathbf{j}^{\mathrm{T}})/|\mathbf{E}^{\mathrm{ext}}|$.

Let us now consider a transformation $\hat{\mathcal{T}}$ for which $\mathbf{E}^{\mathrm{ext}}\mathsf{A} = -\mathbf{E}^{\mathrm{ext}}$ [Eq. (6)]. Right multiplication by A^{T} on both sides yields $\mathbf{E}^{\mathrm{ext}} = -\mathbf{E}^{\mathrm{ext}}\mathsf{A}^{\mathrm{T}}$. Replacing this expression into the component of the current in the direction of the field that we obtained in the previous paragraph results in $(\mathbf{E}^{\mathrm{ext}}\mathsf{A}^{\mathrm{T}})\cdot\mathbf{j}^{\mathrm{T}}/|\mathbf{E}^{\mathrm{ext}}| = -\mathbf{E}^{\mathrm{ext}}\cdot\mathbf{j}^{\mathrm{T}}/|\mathbf{E}^{\mathrm{ext}}| = -j_\parallel$. In summary, the parallel component of the current for applied potentials of $\mathbf{E}^{\mathrm{ext}}$ and $-\mathbf{E}^{\mathrm{ext}}$ are $j_\parallel$ and $-j_\parallel$, respectively; hence $\alpha_{\mathrm{CR}} = 1$. In other words, if the system is invariant upon applying the Euclidean transformation $\hat{\mathcal{T}}$, then CR (for the component of the current in the direction of the field) will not occur for all applied external potentials fulfilling Eq. (6).